Journal of Alloys and Compounds 798 (2019) 53–58

Contents lists available at ScienceDirect

Journal of Alloys and Compounds

journal homepage: http://www.elsevier.com/locate/jalcom

Pt-rich intermetallic APt_8P_2 (A = Ca and La)

Xin Gui [a, *], Zuzanna Sobczak [b], Tomasz Klimczuk [b], Weiwei Xie [a, **]

[a] Department of Chemistry, Louisiana State University, Baton Rouge, LA, 70803, USA
[b] Faculty of Applied Physics and Mathematics, Gdansk University of Technology, Narutowicza 11/12, Gdansk, 80-233, Poland

ARTICLE INFO

Article history:
Received 2 March 2019
Received in revised form
15 May 2019
Accepted 19 May 2019
Available online 21 May 2019

Keywords:
$CaPt_8P_2$
$LaPt_8P_2$
Solid-state synthesis
Heat capacity
Bonding analysis

ABSTRACT

The combination of experimental and theoretical investigation of two new Pt-rich intermetallic compounds: APt_8P_2 (A = Ca and La) is presented, including solid-state synthesis, crystal structure determination, physical properties characterization and chemical bonding analysis. APt_8P_2 was obtained through the high-temperature pellet synthesis. According to both single crystal and powder X-ray diffraction results, APt_8P_2 crystallize in the monoclinic $DyPt_8P_2$-type structure with space group $I2/m$ (S.G. 12). Crystal structure of APt_8P_2 can be considered as intercalating multiple Pt layers into APt_2P_2. Magnetic susceptibility measurement indicates diamagnetism of both compounds. The specific heat down to 1.8 K shows no evidence for bulk superconductivity in either $CaPt_8P_2$ and $LaPt_8P_2$. Electronic structure calculations match well with the observed structural stability and metallic behavior. The following Crystal Orbital Hamiltonian Population (-COHP) calculations suggest that the difference of Pt-Pt antibonding interaction could be the key factor that results in the shrinkage of c axis in APt_8P_2.

1. Introduction

Platinum-based intermetallic compounds are attractive in materials science due to a variety of applications such as heterogeneous catalysis and new superconductors [1–7]. Pt-based superconducting materials receive remarkable attention for their unique properties, especially the unconventional mechanism behind the electron-phonon coupling and the coexistence of superconductivity and other physical phenomena (Charge-Density-Waves (CDWs), magnetism et al.) [8–25]. For example, the first heavy-fermion superconductor with non-centrosymmetric crystal structure was discovered in $CePt_3Si$ with $T_c \sim 0.75$ K [15]. Another heavy-fermion superconductor UPt_3 shows multiple distinct superconducting phases [14,26]. Recent study on layered $SrPt_2As_2$ with coexistence of superconductivity and CDWs shows that the local split distortions of Pt atoms in PtAs layers plays a critical role in driving the CDW instability as well as enhancing the superconductivity by softening phonon [27,28]. In addition to these unconventional superconductors, there are also interesting Pt-rich superconductors, for example, noncentrosymmetric Li_2Pt_3B and $LaPt_3Si$ [16,17]. Recently, a series of Pt-rich antiperovskite-type intermetallic compound, APt_3P (A = Ca, Sr and La), which is closely related to $CePt_3Si$, were found to host strong coupling superconductivity with T_c up to 8.4 K [29]. In 2016, Nishii's group synthesized a new superconductor $LaPt_5As$ at 10 GPa and the superconducting temperature of $LaPt_5As$ is 2.6 K [30]. The density functional theory (DFT) calculations of $LaPt_5As$ indicate that Pt layers play a significant role in transporting the superconducting current in the layered phase.

Herein, we report the synthesis of two newly-discovered Pt-rich intermetallic compounds APt_8P_2 (A = Ca and La) with the same structure type as reported $DyPt_8P_2$ [31]. The heat capacity measurement shows no superconductivity down to 1.8 K. The bond analysis suggests that the difference of Pt-Pt antibonding interaction could lead to the shrinkage of c axis in APt_8P_2 rather than bulk superconductivity based on the hypothesis in our previous superconducting $BaPt_2Bi_2$ paper that the strong antibonding interactions may be critical for the superconducting state [32].

2. Experimental section

2.1. Preparation of polycrystalline samples of Ca(La)Pt_8P_2

The polycrystalline samples of Ca(La)Pt_8P_2 are produced *via* traditional solid-state method. Elemental calcium (>99.99%, granules, Beantown Chemical)/lanthanum (≥99.9%, <200 mesh, Alfa Aesar), platinum (99.98%, ~60 mesh, Alfa Aesar) and red

* Corresponding author.
** Corresponding author.
E-mail addresses: xgui2@lsu.edu (X. Gui), weiweix@lsu.edu (W. Xie).

https://doi.org/10.1016/j.jallcom.2019.05.239
0925-8388/

phosphorus (99%, ~100 meshes, Beantown Chemical) were put into an alumina crucible with the molar ratio of 1:5:1. An evacuated glass tube with crucible inside was heated to 1050 °C in a Thermal Scientific furnace and stay for 2 days. The furnace was turned off after heating treatment and the tube was air-quenched. A piece of metal-like chunk was obtained and stored in glovebox.

2.2. Phase identification and structure determination

A Rigaku MiniFlex 600 powder X-ray diffractometer (XRD) equipped with Cu K_α radiation ($\lambda = 1.5406$ Å, Ge monochromator) was applied to determine the phases of $CaPt_8P_2$ and $LaPt_8P_2$. Scanning angle was set between 5 and 90° with a step of 0.005° at a rate of 0.08°/min. The powder XRD patterns are fitted by Rietveld method in Fullprof with the use of calculated pattern from single crystal data [33].

Multiple pieces of crystals were measured under room temperature by a Bruker Apex II diffractometer equipped with Mo radiation ($\lambda_{K\alpha} = 0.71073$ Å). Samples protected by glycerol were mounted on a Kapton loop. Seven different positions selected by Bruker APEX3 software were utilized to determine a detailed set of data. The measurement was performed with an exposure time of 10 s per image and a scanning 2θ width of 0.5°. Structure solving was carried out by using direct methods and full-matrix least-squares on F^2 models with SHELXTL package [34]. Data acquisition was made *via* Bruker SMART software with the corrections on Lorentz and polarization effect done by SAINT program. Numerical absorption corrections were accomplished with *XPREP*, which is based on the face-index modeling [35,36].

2.3. Physical properties measurement

The measurement was performed by using Physical Property Measurement System (Quantum Design PPMS). A standard relaxation calorimetry method was used and the data were collected in zero magnetic field between 1.85 K and 300 K. The measurement was performed by using ACMS option of Physical Property Measurement System (Quantum Design PPMS) in DC mode with applied magnetic field of 9 T.

2.4. Electronic structure calculations

2.4.1. Tight-Binding, Linear Muffin-Tin Orbital-Atomic Spheres Approximation (TB-LMTO-ASA)

Tight-Binding, Linear Muffin-Tin Orbital-Atomic Spheres Approximation (TB-LMTO-ASA) using the Stuttgart code was applied to calculate Crystal Orbital Hamiltonian Population (-COHP) curves which are able to identify bonding/antibonding interaction for compounds [37–39]. All integrated values were generated with a convergence criterion of 0.05 meV and a mesh of 164 *k* points [40]. In the ASA method, overlapping Wigner-Seitz (WS) spheres were employed to filled the space where the symmetry of the potential is treated as spherical with a combined correction on the overlapping part. The WS radii are: 2.148 Å for Ca; 2.171 Å for La; 1.363 Å for Pt; and 1.278 Å for P. Empty spheres are required for the calculation, and the overlap of WS spheres is limited to no larger than 16%. The basis set for the calculations included Ca: 4*s*, 4*p*, 3*d*; La: 6*s*, 6*p*, 5*d*, 4*f*; Pt: 6*s*, 6*p*, 5*p*, 5*d*; and P: 3*s*, 3*p*, 3*d* wavefunctions. The 4*p* orbital of Ca, 6*p* orbital of La, 5*p* orbital of Pt and 3*d* orbital of P atoms are automatically downfolded determined by TB-LMTO-ASA program.

2.4.2. Electronic structure calculations

The band structure and density of states (DOS) of $Ca(La)Pt_8P_2$ were calculated using the WIEN2k code, which has the full-potential linearized augmented plane wave method (FP-LAPW) with local orbitals implemented [41,42]. The structural lattice parameters obtained from experiments are used for the calculation. For treatment of the electron correlation within the generalized gradient approximation, the electron exchange-correlation potential was used with the parametrization by Perdew et al. (i.e. the LDA) [43]. The conjugate gradient algorithm was applied and the energy cutoff was 500 eV. Reciprocal space integrations were completed over a $10 \times 5 \times 10$ Monkhorst-Pack *k*-points mesh [44]. With these settings, the calculated total energy converged to less than 0.1 meV per atom.

3. Results and discussion

3.1. Crystal structure, phase and chemical composition determination

Crystal structures of APt_8P_2 (A = Ca & La) have been determined identical with $DyPt_8P_2$, the only reported compound holding this structure type [31]. Both $CaPt_8P_2$ and $LaPt_8P_2$ crystallize in space group $I\,2/m$ (S. G. 12). The crystallographic data are listed in Tables 1 and 2 & Table S1 in Supporting Information. It can be found that with the substitution of M atoms from Ca (180 p.m.), which has a smaller atomic radius, to La (195 p.m.), which has a larger atomic radius, the lattice parameters of *a* & *b* and the unit cell's volume were increasing [45]. However, the unit cell shrinks along *c*-axis in $LaPt_8P_2$. The possible reason for this will be discussed in the bonding analysis part. As shown in Fig. 1(A), the major frame of $Ca(La)Pt_8P_2$ is constructed by the repeating units enclosed in red lines which is infinite along *b*-axis. The repeating unit can be described as *Pt4-P6* layer sandwiched by two *Pt1-Pt2-Pt3* layers. Ca/La atoms are embedded inside the holes between every two repeating units and collinear with two circled Pt4 atoms.

The phases of both samples are determined by Rietveld refinement performed in Fullprof suite. The powder X-ray diffraction (PXRD) pattern of $CaPt_8P_2$, as shown in Fig. 1(B), indicates that a nearly pure phase was obtained based on the high-quality fitting. According to Fig. 1(C), some undefined peaks were found which implies impurities in $LaPt_8P_2$ batch. However, majority peaks of $LaPt_8P_2$ can be fitted with the calculated pattern. Therefore, we can basically tell that both crystal structures are consistent with the PXRD pattern.

3.2. Physical properties measurements of $Ca(La)Pt_8P_2$

Fig. 2 shows results of the heat capacity (C_p) measurements, plotted as C_p/T *vs* T^2, for $CaPt_8P_2$ and $LaPt_8P_2$. Temperature

Table 1
Single crystal crystallographic data for APt_8P_2 (A = Ca and La) at 293 (2) K.

Refined Formula	$CaPt_8P_2$	$LaPt_8P_2$
F.W. (g/mol)	1662.66	1761.57
Space group; Z	$I\,2/m$; 2	$I\,2/m$; 2
a(Å)	9.221 (1)	9.296 (2)
b(Å)	4.015 (1)	4.081 (1)
c(Å)	9.669 (2)	9.668 (2)
β (°)	102.85 (3)	102.06 (3)
V (Å^3)	349.0 (1)	358.6 (1)
Extinction Coefficient	0.00032 (4)	0.00168 (9)
θ range (deg)	2.761–33.192	2.765–33.084
No. reflections; R_{int}	4023; 0.0466	4118; 0.0524
No. independent reflections	749	759
No. parameters	36	36
R_1: ωR_2 (all *I*)	0.0273; 0.0575	0.0264; 0.0675
Goodness of fit	1.027	1.175
Diffraction peak and hole (e$^-$/Å^3)	3.616; −3.688	4.542; −6.744

Table 2
Atomic coordinates and equivalent isotropic displacement parameters of APt_8P_2 (A = Ca, La) system under different pressures (U_{eq} is defined as one-third of the trace of the orthogonalized U_{ij} tensor ($Å^2$)).

Atom	Wyckoff.	Occ.	*x*	*y*	*z*	U_{eq}
$CaPt_8P_2$:						
Pt1	2*c*	1	0.3318 (1)	0	0.1786 (1)	0.0048 (1)
Pt2	2*c*	1	0.3447 (1)	0	0.4724 (1)	0.0047 (1)
Pt3	2*c*	1	0.0147 (1)	0	0.1636 (1)	0.0046 (1)
Pt4	2*c*	1	0.6435 (1)	0	0.2358 (1)	0.0052 (1)
Ca5	2*c*	1	½	½	0	0.0076 (8)
P6	2*c*	1	0.2364 (4)	0	0.9408 (4)	0.0054 (7)
$LaPt_8P_2$:						
Pt1	2*c*	1	0.3305 (1)	0	0.1785 (1)	0.0001 (1)
Pt2	2*c*	1	0.3451 (1)	0	0.4711 (1)	0.0001 (1)
Pt3	2*c*	1	0.0168 (1)	0	0.1652 (1)	0.0001 (1)
Pt4	2*c*	1	0.6433 (5)	0	0.2360 (1)	0.0002 (1)
La5	2*c*	1	½	½	0	0.0003 (2)
P6	2*c*	1	0.2297 (4)	0	0.9392 (4)	0.0002 (6)

dependence of C_p between 1.85 K and 300 K are shown in FIG. S1 in Supporting Information. In both samples, no clear anomaly of the specific heat was observed implying that both compounds are not superconductors above 1.85 K. The low temperature (1.85 K < T < 30 K) experimental data were fitted using the formula $C_p/T = \gamma+\beta T^2$, where the first and the second parameters are the electronic and the lattice contribution to the specific heat, respectively. The fits yield $\gamma(CaPt_8P_2) = 13.6$ (2) mJ mol^{-1} K^{-2}, $\gamma(LaPt_8P_2) = 15.5$ (2) mJ mol^{-1} K^{-2}, and $\beta(CaPt_8P_2) = 1.304$ (9) mJ mol^{-1} K^{-4}, $\beta(LaPt_8P_2) = 1.113$ (8) mJ mol^{-1} K^{-4}. With the use of equation:

$$\Theta_D = \left(\frac{12\pi^4}{5\beta}nR\right)^{\frac{1}{3}}$$

where R = 8.31 J mol^{-1} K^{-1} and n = 11 for Ca(La)Pt_8P_2, we can find

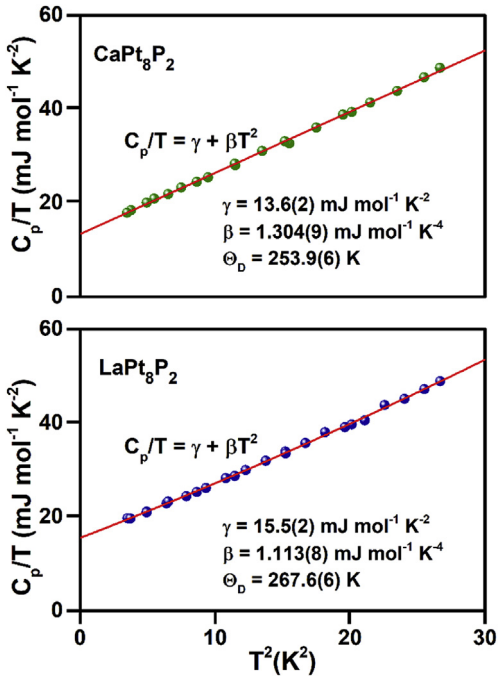

Fig. 2. Heat capacity C_p/T *vs* T^2 without applied field measurements for $CaPt_8P_2$ (top panel) and $LaPt_8P_2$ (lower panel). The red solid line represents the fitting of $C_p/T = \gamma + \beta T^2$. (For interpretation of the references to colour in this figure legend, the reader is referred to the Web version of this article.)

the Debye temperature of Θ_D ($CaPt_8P_2$) = 253.9 (6) K, Θ_D ($LaPt_8P_2$) = 267.6 (6) K. Due to the higher fitted Debye temperature, we can determine that the atoms in $LaPt_8P_2$ should be harder to vibrate and the interaction between atoms in $LaPt_8P_2$ is stronger

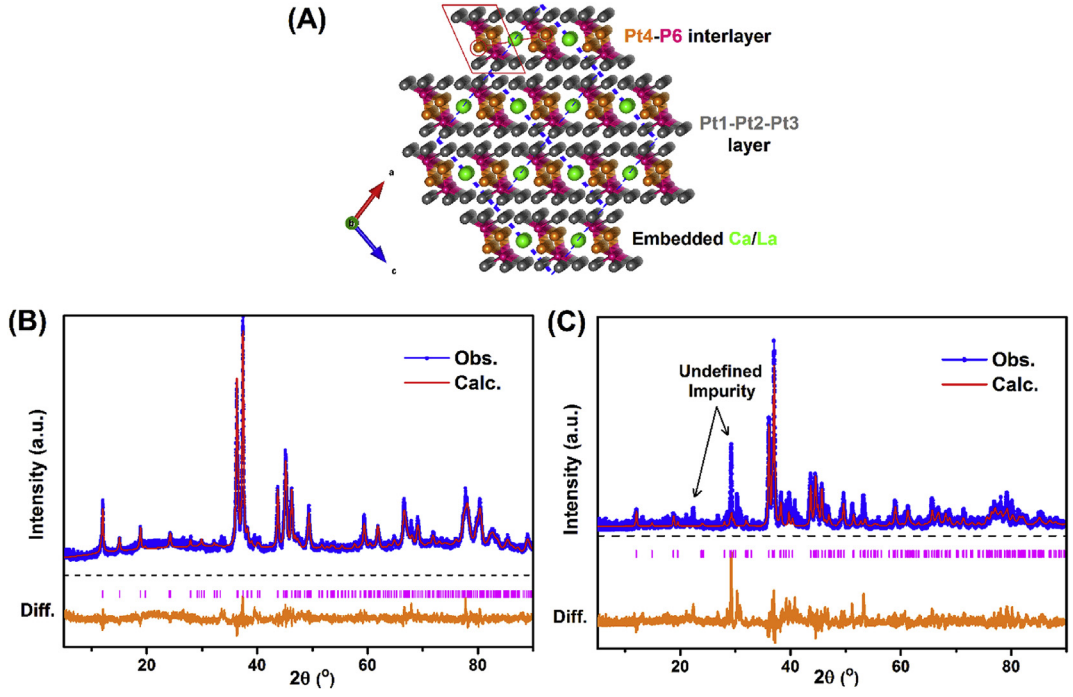

Fig. 1. (A). Crystal structure of Ca(La)Pt_8P_2. Green, grey, orange and pink balls represent Ca(La), Pt1/Pt2/Pt3, Pt4 and P atoms, respectively. **(B).** Powder X-ray diffraction (XRD) pattern of $CaPt_8P_2$ fitted by Rietveld method. **(C).** Rietveld fitting of powder XRD pattern for $LaPt_8P_2$. (For interpretation of the references to colour in this figure legend, the reader is referred to the Web version of this article.)

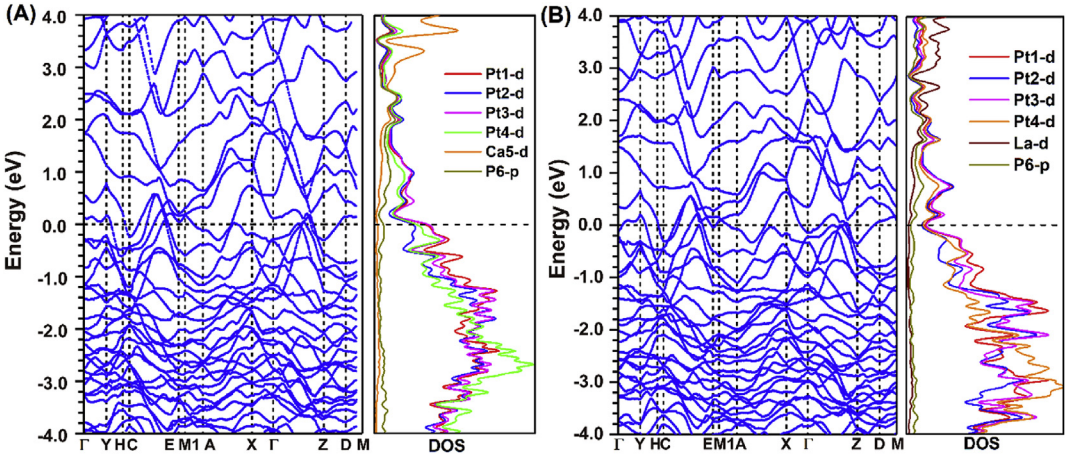

Fig. 3. Band structure and density of states with consideration of SOC effect of Ca(La)Pt_8P_2. **(A).** $CaPt_8P_2$; **(B).** $LaPt_8P_2$.

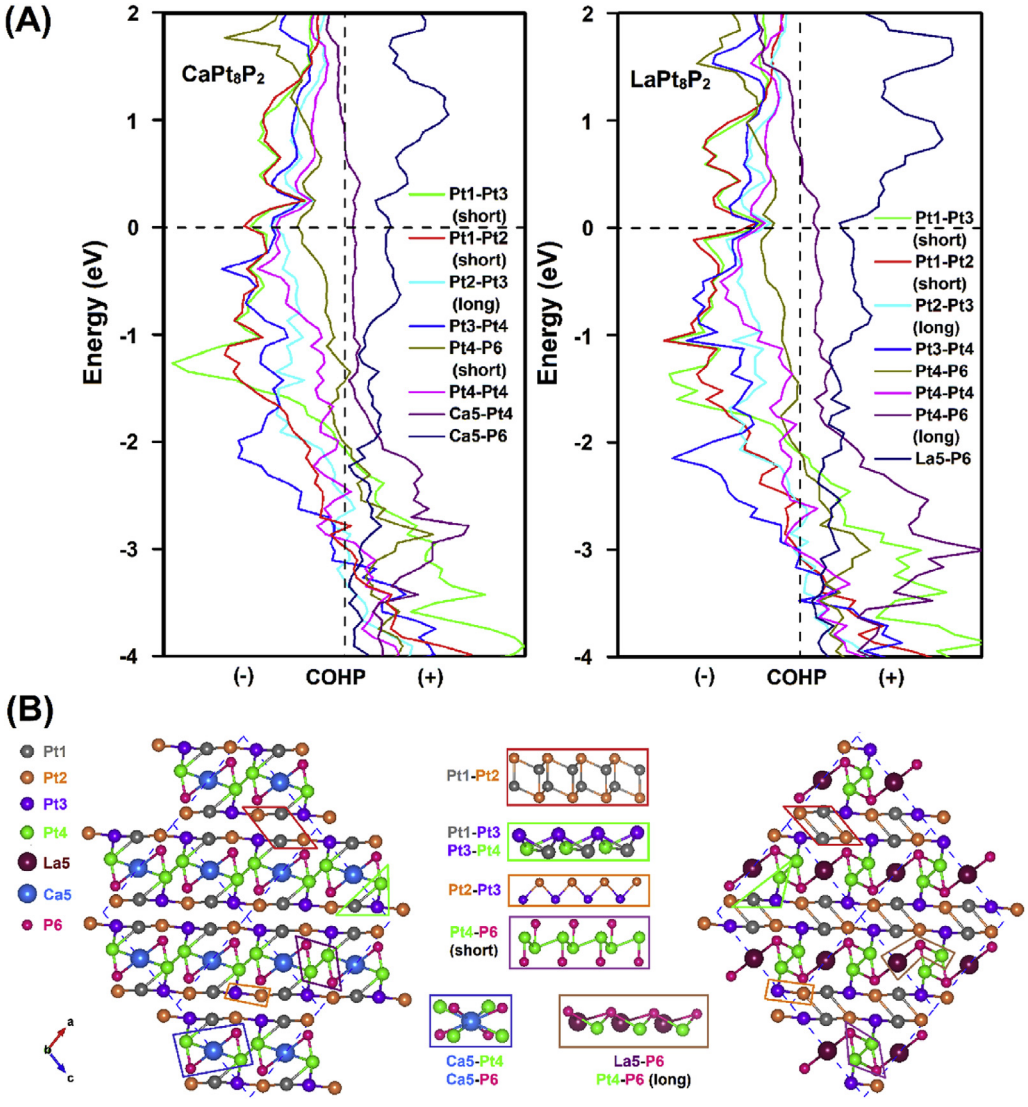

Fig. 4. . (A). Crystal Orbital Hamiltonian Population (-COHP) curves of major interatomic interactions in Ca(La)Pt_8P_2. **(B).** Visualization of major bonding/antibonding interaction in crystal structure.

Table 3
COHP order near Fermi level for both antibonding/bonding parts in Ca(La)Pt_8P_2.

	Order	$CaPt_8P_2$	$LaPt_8P_2$
Antibonding	1st	Pt1-Pt2 (short)	Pt1-Pt2 (short)
	2nd	Pt1-Pt3 (short)	Pt1-Pt3 (short)
	3rd	Pt3-Pt4	Pt3-Pt4
	4th	Pt2-Pt3 (long)	Pt4-Pt4
	5th	Pt4-Pt4	Pt2-Pt3 (long)
	6th	Pt4-P6 (short)	Pt4-P6 (short)
Bonding	1st	Ca5-P6	La5-P6
	2nd	Ca5-Pt4	Pt4-P6 (long)

than that in $CaPt_8P_2$, which will be further explained in bonding analysis part.

Temperature dependence of magnetic susceptibility measured under magnetic field $\mu_0H = 9$ T for $LaPt_8P_2$ and $CaPt_8P_2$ is presented in FIG. S2. Both compounds show diamagnetic behavior down to 1.9 K.

3.3. Band structure & density of states (DOS) of Ca(La)Pt_8P_2

The band structure and density of states (DOS) of both compounds with considering spin-orbit coupling (SOC) effect are presented in Fig. 3. The conventional unit cells were used to construct reciprocal lattice. The *f* orbitals of La atoms were included in the band structure near 3.0 eV but omitted in DOS due to its less significance and larger scale relative to other orbitals. Both band structure and DOS are with the same pattern for both compounds except that the Fermi level moves up in $LaPt_8P_2$ because of more electrons in La atoms. The *d* orbitals of Pt atoms contribute the most around and below the Fermi level.

3.4. Bonding analysis of Ca(La)Pt_8P_2

The results of Crystal Orbital Hamiltonian Population (-COHP) calculation for major interactions of APt_8P_2 and the visualization of bonds are shown in Fig. 4(A) and (B). Six major antibonding interactions and two significant bonding interactions in each compound were selected into comparison. The order of COHP for Ca(La)Pt_8P_2 near E_F is listed from the most-to the least contributed ones in Table 3. When there are two types of bonds between two atoms, they are labelled according to their relative bond lengths (long or short).

3.4.1. Antibonding part

Pt1-Pt2 interaction are the most dominant antibonding components. There are mainly two types of *Pt1-Pt2* interaction which are *Pt1-Pt2* dimer and *Pt1-Pt2* zig-zag chain. In $CaPt_8P_2$, *Pt1-Pt2* zig-zag chain with a shorter bond length, which is located within the repeating unit, contributes the most. However, the *Pt1-Pt2* dimer in $LaPt_8P_2$, which is with short bond length locating between *Pt1-Pt2-Pt3* layers, becomes the most significant antibonding interaction. Regarding the bond length of *Pt1-Pt2* dimer, the one in $LaPt_8P_2$ is shorter than that in $CaPt_8P_2$ which implies a stronger "interlayer" interaction. This can be supported by the integrated COHP (ICOHP) and ICOHP% value, which indicate the bond strength and the percentage of bond strength among all bonds, that ICOHP (ICOHP%) of *Pt1-Pt2* dimer in $LaPt_8P_2$ is 2.044 (5.55%) vs 0.58 (1.80%) for the one in $CaPt_8P_2$ around Fermi level (E_F). Since *Pt1-Pt2* dimer is along *c*-axis, it can be speculated that the stronger *Pt1-Pt2* dimer should be the reason why latter parameter *c* in $LaPt_8P_2$ is smaller than that in $CaPt_8P_2$.

Pt1-Pt3/*Pt3-Pt4* zig-zag chains locate within the repeating unit and are the second/third most dominate antibonding interaction for both $CaPt_8P_2$ and $LaPt_8P_2$. Considering that the ICOHP% of *Pt4-P6* in $CaPt_8P_2$ (9.16%) is larger than that in $LaPt_8P_2$ (7.51%), we can conclude that there are more bonding components in *Pt4-P6*. Therefore, more electrons of Pt4 atoms are distributing in bonding orbitals so that less electrons can be assigned to *Pt4-Pt4* antibonding part. This is the reason why antibonding *Pt2-Pt3* zig-zag chains contribute more at E_F than *Pt4-Pt4* in $CaPt_8P_2$ while the order is reverse in $LaPt_8P_2$.

3.4.2. Bonding part

Ca(La)-P bonds are the strongest bonding interaction around E_F to stabilize the structure. *Ca5-Pt4* nets are the second strongest bonding interaction in $CaPt_8P_2$. However, *La5-Pt4* in $LaPt_8P_2$ is antibonding near E_F. This may due to the fact that with +2 valence state, La has one more outermost electron to bond with surrounding atoms so that more electrons can be assigned to *La5-Pt4* antibonding orbitals. Therefore, *La5-Pt4* antibonding interaction can promote the bonding part of *Pt4-P6* (long) since more electrons can distribute between the longer *Pt4-P6* bond [46]. Moreover, the total ICOHP value of $LaPt_8P_2$ is 36.86 eV while that of $CaPt_8P_2$ is only 32.41 eV, which indicates that the total bonding strength in $CaPt_8P_2$ is not as strong as $LaPt_8P_2$, which further verified the higher Debye temperature and the lower mobility of atoms in $LaPt_8P_2$.

4. Conclusion

Two new Pt-rich intermetallic compounds, $CaPt_8P_2$ and $LaPt_8P_2$, were synthesized and the heat capacity measurements show no transition peaks between 2 and 300 K which indicates there is no superconductivity in both samples above 2 K. The band structure and DOS suggest that *d* orbitals in Pt atoms are dominant near the Fermi level. According to COHP calculation, we conclude that the difference of both types of *Pt1-Pt2* antibonding interaction could be the reason why the lattice parameter *c* of $LaPt_8P_2$ is shorter than that of $CaPt_8P_2$.

Acknowledgements

This research at Department of Chemistry, LSU was supported by Beckman Young Investigator (BYI) Award. X.G. is supported by the National Science Foundation under NSF-OIA-1832967. TK and ZS gratefully acknowledge the financial support from National Science Centre (Poland), Grant No. UMO-2015/19/B/ST3/03127.

Appendix A. Supplementary data

Supplementary data to this article can be found online at https://doi.org/10.1016/j.jallcom.2019.05.239.

References

[1] R.N. Shelton, Superconductivity and crystal structure of a new class of ternary platinum borides, J. Less-Common Met. 62 (1978) 191–196.
[2] S. Moehlecke, D.E. Cox, A.R. Sweedler, The effects of neutron irradiation on the superconducting properties of Nb_3Pt, J. Less-Common Met. 62 (1978) 111–118.
[3] A.L. Ivanovskii, Platinum-based and platinum-doped layered superconducting materials: synthesis, properties and simulation, Platinum Metals Rev 57 (2013) 87–100.
[4] K. Nozawa, N. Endo, S. Kameoka, A.P. Tsai, Y. Ishii, Catalytic properties dominated by electronic structures in PdZn, NiZn, and PtZn intermetallic compounds, J. Phys. Soc. Jpn. 80 (2011), 064801.
[5] E.C. Wegener, Z. Wu, H.-T. Tseng, J.R. Gallagher, Y. Ren, R.E. Diaz, F.H. Ribeiro, J.T. Miller, Structure and reactivity of Pt–In intermetallic alloy nanoparticles: highly selective catalysts for ethane dehydrogenation, Catal. Today 299 (2018) 146–153.
[6] R.D. Cortright, J.A. Dumesic, Microcalorimetric, spectroscopic, and kinetic studies of silica supported Pt and Pt/Sn catalysts for isobutane dehydrogenation, J. Catal. 148 (1994) 771–778.

[7] R.D. Cortright, J.M. Hill, J.A. Dumesic, Selective dehydrogenation of isobutane over supported Pt/Sn catalysts, Catal. Today 55 (2000) 213–223.
[8] W. Wendler, T. Herrmannsdörfer, S. Rehmann, F. Pobell, Electronic and nuclear magnetism in $PtFe_x$ at milli-, and nanokelvin temperatures, Europhys. Lett. 38 (1997) 619.
[9] A.C. Clark, K.K. Schwarzwälder, T. Bandi, D. Maradan, D.M. Zumbühl, Method for cooling nanostructures to microkelvin temperatures, Rev. Sci. Instrum. 81 (2010) 103904.
[10] R. König, A. Schindler, T. Herrmannsdörfer, Superconductivity of compacted platinum powder at very low temperatures, Phys. Rev. Lett. 82 (1999) 4528.
[11] A. Schindler, R. König, T. Herrmannsdörfer, H.F. Braun, Inter-and intragranular effects in superconducting compacted platinum powders, Phys. Rev. B 62 (2000) 14350.
[12] A. Schindler, R. König, T. Herrmannsdörfer, H.F. Braun, G. Eska, D. Günther, M. Meissner, M. Mertig, R. Wahl, W. Pompe, T_c-enhancement in superconducting granular platinum, Europhys. Lett. 58 (2002) 885.
[13] I. Martin, D. Podolsky, S.A. Kivelson, Enhancement of superconductivity by local inhomogeneities, Phys. Rev. B 72 (2005), 060502.
[14] R. Joynt, L. Taillefer, The superconducting phases of UPt_3, Rev. Mod. Phys. 74 (2002) 235.
[15] E. Bauer, G. Hilscher, H. Michor, C. Paul, E.W. Scheidt, A. Gribanov, Y. Seropegin, H. Noël, M. Sigrist, P. Rogl, Heavy fermion superconductivity and magnetic order in noncentrosymmetric $CePt_3Si$, Phys. Rev. Lett. 92 (2004), 027003.
[16] K.V. Samokhin, V.P. Mineev, Gap structure in noncentrosymmetric superconductors, Phys. Rev. B 77 (2008) 104520.
[17] Y. Aoki, A. Sumiyama, M. Shiotsuki, G. Motoyama, A. Yamaguchi, Y. Oda, T. Yasuda, R. Settai, Yo. Ōnuki, Josephson effect between noncentrosymmetric $LaPt_3Si$ and a conventional superconductor, J. Phys. Soc. Jpn. 79 (2010) 124707.
[18] T. Scheler, O. Degtyareva, M. Marqués, Ch. L. Guillaume, J.E. Proctor, S. Evans, E. Gregoryanz, Synthesis and properties of platinum hydride, Phys. Rev. B 83 (2011) 214106.
[19] X. Zhou, A.R. Oganov, X. Dong, L. Zhang, Y. Tian, H.-T. Wang, Superconducting high-pressure phase of platinum hydride from first principles, Phys. Rev. B 84 (2011), 054543.
[20] G. Gao, H. Wang, L. Zhu, Y. Ma, Pressure-induced formation of noble metal hydrides, J.Phys. Chem. C 116 (2012) 1995–2000.
[21] C. Zhang, X.-J. Chen, H.-Q. Lin, Phase transitions and electron–phonon coupling in platinum hydride, J. Phys. Condens. Matter 24 (2011), 035701.
[22] R. Gumeniuk, W. Schnelle, H. Rosner, M. Nicklas, A. Leithe-Jasper, Y. Grin, Superconductivity in the platinum germanides MPt_4Ge_{12} (M= Rare– earth or alkaline-earth metal) with filled skutterudite structure, Phys. Rev. Lett. 100 (2008), 017002.
[23] E. Bauer, X.-Q. Chen, P. Rogl, G. Hilscher, H. Michor, E. Royanian, R. Podloucky, G. Giester, O. Sologub, A.P. Gonçalves, Superconductivity and spin fluctuations in $\{Th,U\}Pt_4Ge_{12}$ skutterudites, Phys. Rev. B 78 (2008), 064516.
[24] R. Gumeniuk, H. Rosner, W. Schnelle, M. Nicklas, A. Leithe-Jasper, Y. Grin, Optimization of the superconducting transition temperature of the filled skutterudite $BaPt_4Ge_{12}$ by gold substitution, Phys. Rev. B 78 (2008), 052504.
[25] D. Kaczorowski, V.H. Tran, Superconductivity in the actinoid-bearing filled skutterudite $ThPt_4Ge_{12}$, Phys. Rev. B 77 (2008) 180504.
[26] G.R. Stewart, Z. Fisk, J.O. Willis, J.L. Smith, Possibility of coexistence of bulk superconductivity and spin fluctuations in UPt_3, in: Ten Years of Superconductivity: 1980–1990, Springer, Dordrecht, 1984, pp. 85–88.
[27] A. Imre, A. Hellmann, G. Wenski, J. Graf, D. Johrendt, A. Mewis, Inkommensurabel modulierte Kristallstrukturen und Phasenumwandlungen—Die Verbindungen $SrPt_2As_2$ und $EuPt_2As_2$, Z. Anorg. Allg. Chem. 633 (2007) 2037–2045.
[28] K. Kudo, Y. Nishikubo, M. Nohara, Coexistence of superconductivity and charge density wave in $SrPt_2As_2$, J. Phys. Soc. Jpn. 79 (2010) 123710.
[29] T. Takayama, K. Kuwano, D. Hirai, Y. Katsura, A. Yamamoto, H. Takagi, Strong coupling superconductivity at 8.4 K in an antiperovskite phosphide $SrPt_3P$, Phys. Rev. Lett. 108 (2012) 237001.
[30] M. Fujioka, M. Ishimaru, T. Shibuya, Y. Kamihara, C. Tabata, H. Amitsuka, A. Miura, M. Tanaka, Y. Takano, H. Kaiju, J. Nishii, Discovery of the Pt-based superconductor $LaPt_5As$, J. Amer. Chem. Soc. 138 (2016) 9927–9934.
[31] A. Imre, A. Mewis, Synthese und Kristallstrukturen von $DyPt_8P_2$ und $Mg_{10-x}Pt_9P_7$, Z. Anorg. Allg. Chem. 634 (2008) 77–81.
[32] X. Gui, L. Xing, X. Wang, G. Bian, R. Jin, W. Xie, Pt–Bi antibonding interaction: the key factor for superconductivity in monoclinic $BaPt_2Bi_2$, Inorg. Chem. 57 (2018) 1698–1701.
[33] J.R. Carvajal, Recent development of the program FULLPROF, Commission on Powder Diffraction (IUCr), Newsletter 26 (2001) 12–19.
[34] G.M. Sheldrick, Crystal structure refinement with SHELXL, Acta Crystallogra. Sec. C 71 (2015) 3–8.
[35] Bruker. Smart, Bruker AXS Inc., Madison, WI, USA, 2012. https://www.bruker.com/products/x-ray-diffraction-and-elemental-analysis/single-crystal-x-ray-diffraction/sc-xrd-software/overview/sc-xrd-software/apex3.html.
[36] N. Walker, D. Stuart, An empirical method for correcting diffractometer data for absorption effects, Acta Cryst 39 (1983) 158–166.
[37] M. Elstner, D. Porezag, G. Jungnickel, J. Elsner, M. Haugk, T. Frauenheim, S. Suhai, G. Seifert, Self-consistent-charge density-functional tight-binding method for simulations of complex materials properties, Phys. Rev. B 58 (1998) 7260.
[38] O.K. Andersen, Ove Jepsen, Explicit, first-principles tight-binding theory, Phys. Rev. Lett. 53 (1984) 2571.
[39] G. Krier, O. Jepsen, A. Burkhardt, O.K. Andersen, The TB-LMTO-ASA Program, 1995. Stuttgart, April.
[40] R. Dronskowski, P.E. Blöchl, Crystal orbital Hamilton populations (COHP): energy-resolved visualization of chemical bonding in solids based on density-functional calculations, J. Phys. Chem. 97 (1993) 8617–8624.
[41] P. Blaha, K. Schwarz, G.K.H. Madsen, D. Kvasnicka, J. Luitz, "wien2k." An Augmented Plane Wave+ Local Orbitals Program for Calculating Crystal Properties, 2001.
[42] E. Wimmer, H. Krakauer, M. Weinert, A.J. Freeman, Full-potential self-consistent linearized-augmented-plane-wave method for calculating the electronic structure of molecules and surfaces: O_2 molecule, Phys. Rev. B 24 (1981) 864.
[43] J.P. Perdew, Y. Wang, Accurate and simple analytic representation of the electron-gas correlation energy, Phys. Rev. B 45 (1992) 13244.
[44] R.D. King-Smith, D. Vanderbilt, Theory of polarization of crystalline solids, Phys. Rev. B 47 (1993) 1651.
[45] F.A. Cotton, G. Wilkinson, Advanced Inorganic Chemistry, fifth ed., Wiley, 1988, ISBN 978-0-471-84997-1, p. 1385.
[46] X. Gui, Z. Sobczak, T.R. Chang, X. Xu, A. Huang, S. Jia, H.T. Jeng, T. Klimczuk, W. Xie, Superconducting SrSnP with strong Sn–P antibonding interaction: is the Sn atom single or mixed valent? Chem. Mater. 30 (2018) 6005–6013.